


Electronic structures and spectroscopic signatures of silicon-vacancy containing nanodiamondsAlessio Petrone, Ryan A. Beck, Joseph M. Kasper, and Xiaosong Li*
*Department of Chemistry, University of Washington, Seattle, Washington 98195, USA*Yue Huang, Matthew Crane, and Peter Pauzauskie
Department of Materials Science and Engineering, University of Washington, Seattle, Washington 98195, USA (Received 27 January 2018; revised manuscript received 5 June 2018; published 8 November 2018)

The presence of midgap states introduced by localized defects in wide-band-gap-doped semiconductors can strongly affect the electronic structure and optical properties of materials, generating a wide range of applications. Silicon-divacancy defects in diamond have been recently proposed for probing high-resolution pressure changes and performing quantum cryptography, making them good candidates to substitute for the more common nitrogen-vacancy centers. Using group-theory and *ab initio* electronic structure methods, the molecular origin of midgap states, zero-phonon line splitting, and size dependence of the electronic transitions involving the silicon-vacancy center is investigated in this paper. The effects of localized defects on the Raman vibrational and carbon *K*-edge x-ray absorption spectra are also explored for nanodiamonds. This paper presents an important analysis of the electronic and vibrational structures of nanosized semiconductors in the presence of midgap states due to localized defects, providing insight into possible mechanisms for modulating their optical properties.

DOI: [10.1103/PhysRevB.98.205405](https://doi.org/10.1103/PhysRevB.98.205405)**I. INTRODUCTION**

Wide-band-gap-doped semiconductors are promising candidates for use in many technological applications since the controlled implantation of localized defects can introduce new electronic levels within the band gap, strongly modifying the material interactions with electromagnetic radiation [1–6]. Diamond presents a large optical band gap for bulk (~ 5.5 eV) [7] and has a very dense lattice that both restricts defect diffusion and restricts phase transitions at high temperatures. Thus, the manipulation and the characterization of isolated defects in diamonds have generated a wide range of applications, such as quantum computing, sensing, and cryptography [8–14].

When the crystal size approaches the nanodimension (~ 5 nm), diamonds no longer express bulk properties. A band-gap opening is observed, and discrete electronic levels (typical of molecules) emerge at the band edges. These are all consequences of the quantum confinement effect [15–18]. Therefore, the interaction between doped diamonds and light may be further modulated by adjusting the host nanocrystal size. Substitutional nitrogen and nitrogen-vacancy (NV) centers are common defects in diamond and have received attention for their sensitive optical and spin properties [8–11, 19–21]. The peculiar low diffusion rate of NV centers enables the optical probing of local variations in time, which can affect the spin precession rate of the defects, making them suitable for quantum sensing applications [14]. Doping introduces new sub-band-gap levels, and it has been shown that NV centers in diamond give rise to new dopant-centered $sp^3 - sp^3$ midgap electronic transitions and charge-transfer

(“photoionization”) excited states [22]. Similar applications in quantum information processing [23] have been shown for the negatively charged silicon-vacancy (SiV^-) center due to its short fluorescent lifetime, narrow emission linewidth, and high percentage of photons (~ 70 – 80%) emitted through its zero-phonon line (ZPL) [24, 25]. This defect has also been shown to be useful as a high-resolution high-pressure sensor [26]. Doped diamond-based pressure probes can function at higher pressures than the currently used ruby sensors as the rigid diamond lattice is still present above 100 GPa, whereas ruby undergoes a phase transition.

The SiV center can exist as either a neutral triplet in its ground state, neutral SiV , or as an anionic doublet state, anionic SiV^- [27–31]. The latter is the most common stable ground-state electronic configuration [32]. Experimentally, the ZPL measured in doped diamonds in the bulk limit is 1.31 and 1.68 eV for the neutral SiV and anionic SiV^- , respectively. Additionally, in SiV^- a blueshift in the zero-phonon line as a function of the decreasing crystal size has been observed for nanodiamonds [33]. For the reduced systems the ZPL splits into a four-line fine-structure at helium temperature [34, 35]. The origin of this fine-structure splitting in the ground and excited states has been explained by dynamic Jahn-Teller and/or by spin-orbit effects [27, 34, 36, 37].

Vibrational spectroscopy can also be used to probe the presence of these defects since the changes in the dipole and the polarizability induced by the dopant can strongly modify the selection rules for the infrared and Raman active modes, respectively. In addition to UV-visible (vis), the *K*-edge x-ray absorption spectrum in diamonds has been proposed to be sensitive to the introduction of dopants [38]. Moreover, carbon *K*-edge spectra in nanodiamonds exhibit unidentified pre-edge features that have been either attributed to the presence

*xсли@uw.edu

of sp^2 carbon atoms lying on the surface as a consequence of the surface reconstruction, or to the introduction of new empty levels within the band gap resulting from impurities [38]. Despite their importance, carbon K -edge x-ray and vibrational transitions for the characterization of SiV centers in nanodiamond along with the effects of the SiV center location in the crystal lattice (i.e., surface effects and symmetry breaking) and system size (i.e., quantum confinement) on the electronic and vibrational excitations have not been well studied. In this paper, theoretical investigations with a finite cluster approach of both the electronic and the vibrational properties are carried out using hybrid density functional theory (DFT) and linear-response time-dependent density functional theory (TDDFT) for a reduced SiV⁻ color center in nanodiamond systems of different sizes. TDDFT, combined with a cluster approach, has shown very promising results for the theoretical characterization of excited states in doped semiconductor quantum dots (in particular, NV-doped nanodiamonds) [22,39–48] and the vibrational/dynamical properties of molecules [49–53]. The work presented herein focuses on the quantum confinement effects on the electronic (UV-vis and x-ray) and vibrational (Raman) spectroscopies on several SiV-doped diamond nanoclusters. The effect of the defect symmetry (or the lack of) as a function of the size is also analyzed.

II. METHODOLOGY

Nearly spherical diamond quantum dots, C₄₄H₄₂ (diameter ~ 0.8 nm), C₁₂₁H₁₀₄ (diameter ~ 1.2 nm), C₁₈₂H₁₄₂ (diameter ~ 1.4 nm), and C₄₈₇H₃₁₀ (diameter ~ 2.1 nm) were used as starting models for the SiV-doped systems. They were constructed using the bulk face-centered cubic lattice parameter [7] $a_0 = 0.357$ nm, and hydrogen atoms were used to passivate the surface dangling bonds, according to the procedure presented in Ref. [22]. The sizes of these quantum dots are similar to the smallest nanodiamonds obtainable by detonation or laser-heated diamond-anvil cell synthesis [12,54–56]. As the diamond excitonic (EXC) Bohr radius is estimated to be ~ 1.6 nm [57], electronic properties of these small diamond quantum dots will exhibit quantum confinement effects.

The SiV center in diamond consists of a silicon atom and a vacancy in a split-vacancy configuration [28,30,58]. The SiV center was created by removing two carbon atoms near the center of the nanodiamonds along the $\langle 1, 1, 1 \rangle$ axis of the models and positioning the silicon at the center of the resulting divacancy in a local D_{3d} environment (namely, SiV *frozen*) as observed in previous computational studies [27,31,59,60]. To evaluate the lattice distortion due to the presence of the SiV center itself, the SiV center and the nearest-neighboring six carbon atoms were fully optimized while maintaining the rest of the diamond structure at the crystal lattice (namely, SiV *relaxed*). These optimization schemes have shown accurate results for describing the lattice distortion of nitrogen-vacancy-doped diamonds of similar sizes [22]. In this paper, we focus on the reduced SiV⁻ center, whose ground state has been shown to be a doublet [32]. The ~ 1.2 -nm reduced SiV⁻ C₁₁₉SiH₁₀₄⁻ was used to estimate the excited-state structural reorganization and relaxation energy.

This system was further optimized according the first bright excited-state energy gradient provided by TDDFT and using the SiV⁻ *relaxed* optimization scheme, described above. The relaxation energy in the excited state was computed as the energy difference between the vertical excitation energy using the ground-state and the excited-state optimized geometries. The ~ 1.2 -nm-diameter pure C₁₂₁H₁₀₄ and the reduced SiV⁻ C₁₁₉SiH₁₀₄⁻ were also further fully optimized in the ground state by relaxing all atoms to perform the vibrational analysis. Geometries were considered fully optimized when both the forces [maximum and root-mean-square (rms) force 0.000 450 and 0.000 300 Hartree/bohr, respectively] and displacement (maximum and rms displacement 0.0018 and 0.0012 bohr, respectively) values for all free atoms were below the threshold criteria.

All calculations were performed using the development version of the GAUSSIAN software package [61]. The ground-state electronic structures were obtained by solving the Kohn-Sham equation using the range-separated version of the hybrid Becke three-parameter Lee-Yang-Parr (B3LYP) density functional [62–64] with the Coulomb-attenuating approach (CAM-B3LYP) [65]. The necessity for using basis sets with large spatial extent (i.e., diffuse functions) has been demonstrated to be important in nanodiamonds since C-H bonds create low-energy empty states that are Rydberg-like, that may reduce the band gap [66,67]. These states can play an important role for shallow implanted NV centers in diamond [68]. On the other hand, diffuse functions have been previously shown to be less important for localized defects located far from the surface [33,69,70]. CAM-B3LYP is known to outperform the canonical hybrid (i.e., B3LYP, Perdew-Burke-Ernzerhof-0 functional, etc.) for the description of the Rydberg-like and charge-transfer states due to their high sensitivity to the treatment of exact exchange [71–73]. Since the presence of these Rydberg-like states can influence the predicted quantum confinement effects, CAM-B3LYP/6-31++G(d, p) was used for this paper. The electronic structures of excited states were calculated using TDDFT within the linear-response framework [74–76] and its energy specific implementation for the high-energy states [77,78].

III. RESULTS AND DISCUSSION

A. Structural reorganization and electronic configurations

The models used in this paper support local symmetry, but they do not preserve a global inversion symmetry operation, therefore the SiV *frozen* conformation has an overall C_{3v} symmetry, given the asymmetry on the nanodiamond surface. Effects of the SiV location in nanodiamonds (i.e., the position of the defect with respect to the surface) can also influence the electronic and optical properties of the systems, and they are separately investigated in detail in the next sections for one of the larger models. Despite this, the models can retain, in the SiV *frozen* conformation, a local symmetric arrangement where all Si-C distances are 1.944 Å and the C-Si-C angles are either 80.9° or 99.1°. The local symmetry of the defect may still be described as C_{3v} plus inversion, retaining a local D_{3d} symmetry [see Fig. 1, panels (a) and (a')].

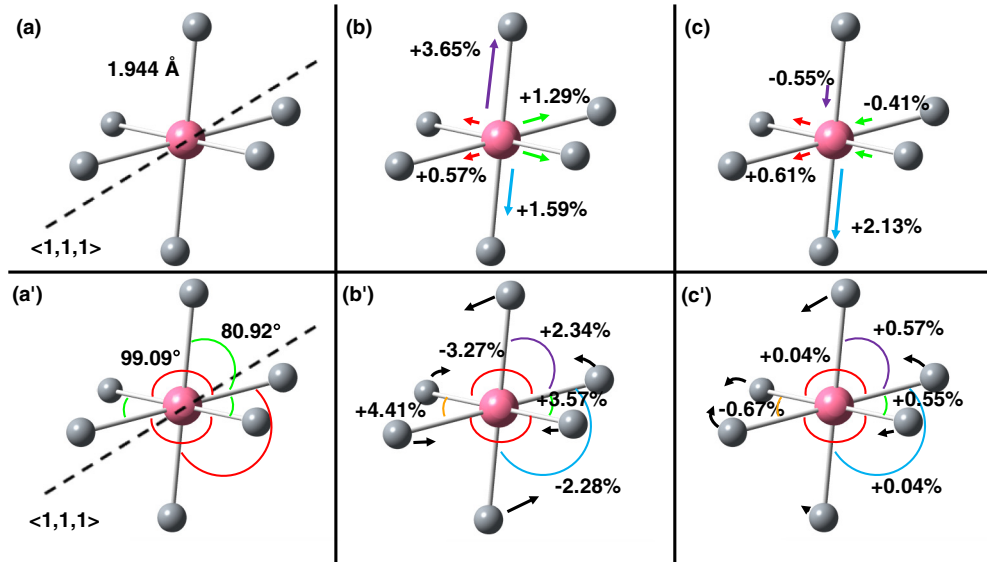


FIG. 1. Geometry relaxation near the SiV center for the ~ 1.2 -nm-diameter reduced $\text{SiV}^- \text{C}_{119}\text{SiH}_{104}^-$ systems: carbon in gray and silicon in pink (only the active atoms during the optimization are reported, see the Methodology section for details). The SiV *frozen* structure with silicon located in a pseudolocal D_{3d} symmetry [panels (a) and (a')] is represented along with the ground- [panels (b) and (b')] and first bright excited-state [panels (c) and (c')] relaxed structures. Both the bond (top panels) and the angle (bottom panels) change in value upon relaxation (according to the procedure detailed in the Methodology section) with respect to the SiV^- *frozen* configuration for the ground state and with respect to the ground-state configuration for the excited state, are reported in percentages in panels (b) and (c), respectively. The same color is used to highlight symmetric changes. The ground-state *relaxed* geometry was also compared with the fully relaxed geometry showing a similar symmetry in the distortion (see Fig. S1 of the Supplemental Material [79]).

The lattice structural reorganization in the electronic ground state in $d \sim 1.2$ -nm SiV-doped nanodiamond is summarized in Fig. 1 [panels (b) and (b')]. A uniform expansion of the Si pocket can be clearly seen from the elongation of all Si-C distances. Upon relaxation on the ground electronic state, the local D_{3d} symmetry is broken, although a pseudo- C_s symmetry can be still observed by inspecting the Si-C distances. When the system is further allowed to relax on the first bright excited state, a nonuniform bond change is observed. Half of the Si-C distances undergo an expansion of the bond length, and the other half undergo a compression [see panel (c) in Fig. 1] compared to the previously examined ground-state relaxed geometry. The calculated relaxation/reorganization energy due to the optical excitation for this size is about 0.01 eV, which is much smaller than the one observed for the NV center (about 0.21 eV). This value agrees with previous calculations on Si-doped diamonds [30] and explains the small contribution of the vibration sideband in the emission spectrum for these systems [32].

Figure 2 shows the total and partial density of states (PDOS) using the calculated molecular orbitals (MOs) with the spin-up and spin-down densities plotted as positive and negative values, respectively. Both the valence band (VB) and the CB consist of carbon p and s characters, whereas multiple levels at the SiV center appear inside the band gap and near the band edges. The VB and CB of the ~ 2.1 -nm-diameter nanodiamond are separated by an energy gap of 5.21 eV. As the system sizes decrease, the band gap increases due to stronger quantum confinement effects.

In the systems containing non interacting SiV centers, the silicon atoms contribute their four valence electrons to the SiV centers. There are also six dangling electrons from the six

nearest-neighbor C atoms to the vacancies, giving rise to a total of 10 electrons at the SiV centers (11 for the reduced system). The local D_{3d} symmetry splits the four sp^3 atomic orbitals of Si to a_{2u} , e_u , a_{1g} , and the six p atomic orbitals of nearby C atoms to e_g , e_u , a_{2u} , and a_{1g} symmetry groups. The symmetry rules dictate that the set of orbitals of e_g symmetry has almost zero overlap with the Si atomic orbitals, resulting in a set of high-energy (and mostly energetically “pinned” in the band gap) MOs with significant contributions from the carbon p orbitals surrounding the silicon (see the colored PDOS in Fig. 2); all other atomic orbitals previously listed (e_g , e_u , a_{2u} , and a_{1g}) can hybridize and form MOs surrounding the defect [depicted in Fig. 3(a)]. The resulting σ bonding and antibonding MOs of a_{2u} and a_{1g} symmetries are energetically buried in the VB and CB, respectively (not shown).

On the other hand, the hybridized bonding MOs of e_u symmetry are the most interesting ones because they are likely responsible for the peculiar optical properties of SiV centers. These molecular orbitals lie at the VB edge (the antibonding ones are energetically located at the CB edge, not represented) and show a reasonable contribution from both the carbon p and the silicon sp^3 orbitals. The resulting MOs show a nonzero overlap with the VB edge of the nanodiamonds, forming a set of three molecular orbitals at the VB edge. Only in the 0.8-nm nanodiamond the MOs of e_u symmetry are energetically well separated from the VB. In this paper, the negatively charged SiV defect ground-state electronic state is 2E_g (in a D_{3d} perfect symmetry), and its electronic configuration can be described as $e_u^4 e_g^3$, where the e_g level is partially filled, in agreement with previous DFT calculations [27,30,80].

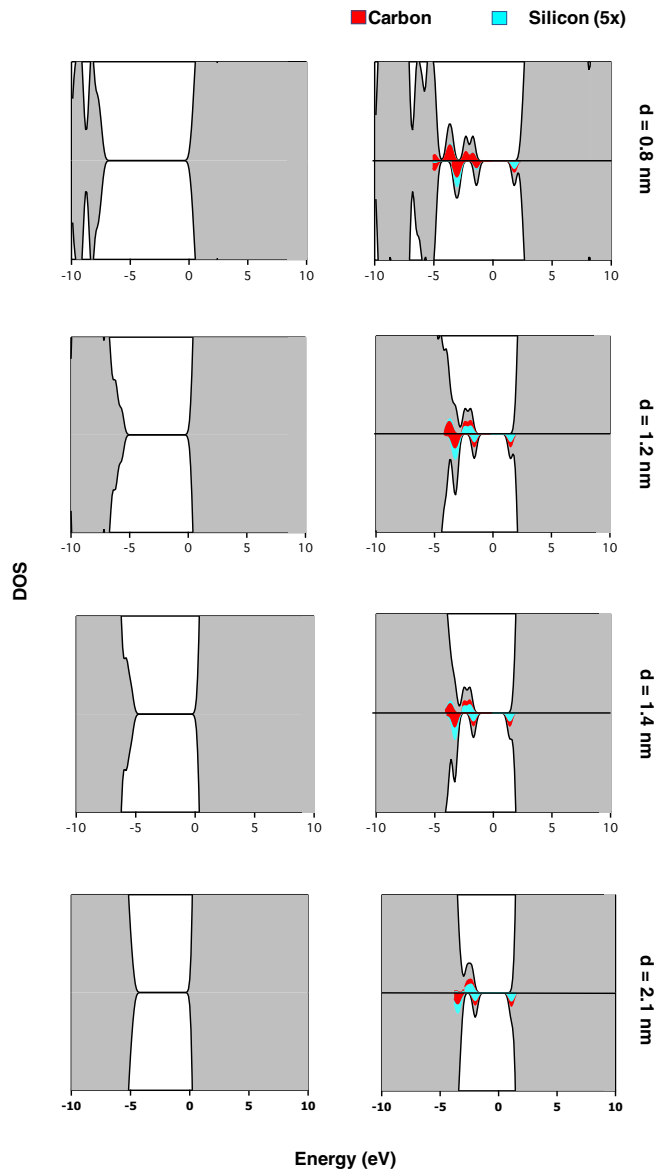


FIG. 2. CAM-B3LYP/6-31 + $G(d, p)$ total and partial densities of states (PDOS) [this last visualized only for Si and its first-neighboring C atom levels within the band gap and the conduction band (CB)]. The red and light blue colored regions show the C $2p$ and Si (magnified by $5\times$) $3s$ and $3p$ contributions to the PDOS diagrams, respectively. Spin up, positive density values; spin down, negative density values. The DOS diagrams are calculated for the pure C_XH_Y and the reduced *frozen* $C_{X-2}SiH_Y^-$ (left and right, respectively) nanodiamonds of increasing sizes ($d \sim 0.8, 1.2, 1.4,$ and 2.1 nm from top to bottom).

B. Midgap optical transitions

As the size of nanodiamond decreases, the quantum confinement effect [18,81] leads to an increase in the band gap [5.21 eV for C_{487} , 5.78 eV for C_{182} , 6.07 eV for C_{121} , and 7.77 eV for C_{44} ; reported as the highest occupied molecular orbital/lowest unoccupied molecular orbital (HOMO/LUMO) differences] as observed in other semiconducting nanocrystals [39,82]. The previously presented electronic structures for anionic SiV⁻ defects in a nanodiamond give rise to

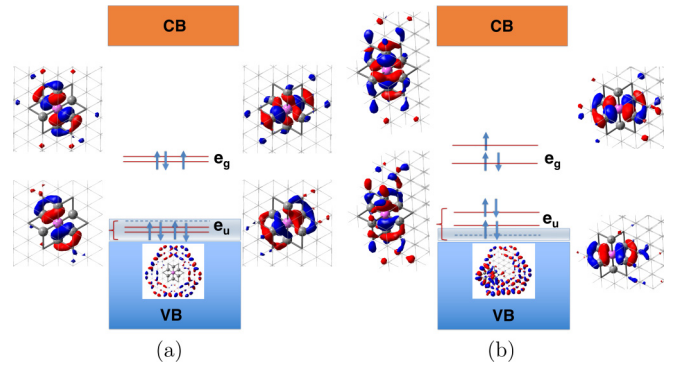


FIG. 3. Schematic of the SiV center electronic layout according to the D_{3d} point-group symmetry. Panel (a) SiV in the center of the nanodiamond and panel (b) where the SiV defect is close to the surface and partially breaks the group symmetry (positions 1 and 4 in Fig. 6, respectively). The zoomed-in $C_{180}SiH_{142}^-$ CAM-B3LYP/6-31 + $G(d, p)$ β MO contour plots with the pseudo- C_{3v} axis parallel to the z axis (entering the figure) are represented. The isodensity values of 0.05, 0.05, and 0.03 are used for the e_g , e_u and VB MO contour plots, respectively. The energetic layout presents an uneven alignment between the α/β filled e_g with respect to the β e_g LUMO, please see Fig. 2 for a more detailed analysis.

several characteristic sets of optical transitions exhibited in the spectroscopic measurement of SiV-containing nanodiamonds. Optical spectra for different-sized SiV⁻ containing nanodiamonds using linear-response TDDFT are reported in Fig. 4. The energy levels of these SiV centers in the diamond lattice are illustrated in Fig. 3(a). This energetic layout leads to unique midgap optical transitions in SiV-containing nanodiamonds.

The optical spectra in Fig. 4 shows a spectroscopic feature between 1.70 and 2.10 eV consisting of two transitions from the two filled MOs of e_u (β) symmetry to the empty e_g (β). Table I lists their vertical excitation energies in various SiV-containing nanodiamonds. These transitions give rise to the

TABLE I. TD-CAM-B3LYP/6-31 + $G(d, p)$ midgap vertical excitation energies (e_u to e_g , β manifold) for the anionic SiV⁻ systems (in eV) and the corresponding oscillator strengths (reported in parentheses). All systems present a dark excited state <100 meV apart from the ground state due to the swap between the occupied and empty e_g orbitals (transitions not shown). We compare results between the SiV *relaxed* (SiV center position is optimized, see the text) with the ones obtained from just inserting the SiV center by replacing the corresponding atoms (SiV *frozen*) in the center of the pure nanodiamond.

| | SiV <i>relaxed</i> | SiV <i>frozen</i> |
|---------------------------------------|--------------------|-------------------|
| SiV ⁻ $C_{42}SiH_{42}^-$ | 1.70(0.077) | 1.63(0.068) |
| | 2.06(0.028) | 1.81(0.014) |
| SiV ⁻ $C_{119}SiH_{104}^-$ | 1.67(0.070) | 1.59(0.061) |
| | 2.09(0.019) | 1.82(0.014) |
| SiV ⁻ $C_{180}SiH_{142}^-$ | 1.59(0.064) | 1.51(0.056) |
| | 1.99(0.021) | 1.90(0.015) |

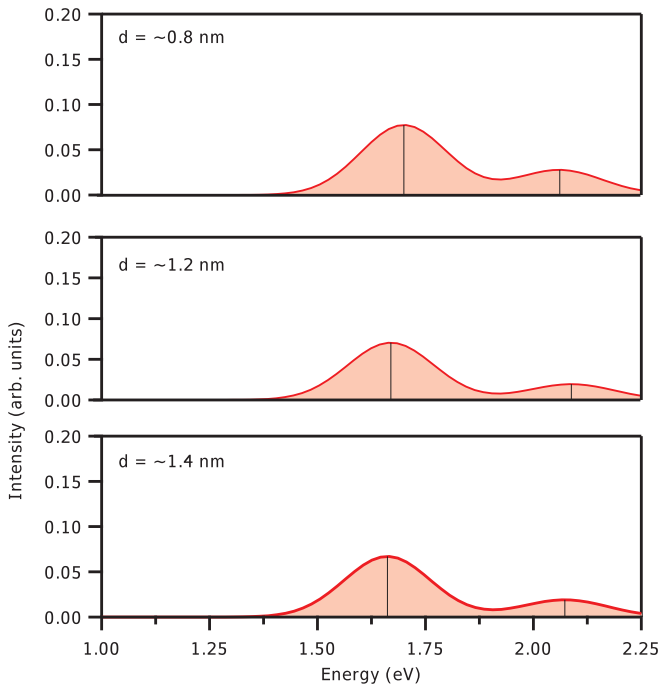


FIG. 4. TD-CAM-B3LYP/6-31 + +G(d, p) UV-vis spectra (only the two first midgap transitions involving the $e_u \rightarrow e_g$ β manifold are reported) for the relaxed anionic $\text{SiV}^- \text{C}_{X-2}\text{SiH}_Y^-$ nanodiamonds as a function of the increasing quantum dot diameter ($d \sim 0.8, 1.2,$ and 1.4 nm from top to bottom). A Gaussian broadening has been applied to the individual transitions labeled with black lines to form the spectrum with a full width half maximum value of 0.10 eV.

experimental ZPL for the ${}^2E_g(e_u^4e_g^3) \rightarrow {}^2E_u(e_u^3e_g^4)$ excitation at 1.686 eV [32], and the main transition contributing to this feature undergoes a small blueshift with diminishing system size (from bottom to top in Fig. 4 and in Table I). The partial charge-transfer characters of the ZPLs in SiV-doped systems are due to the fact that MOs of e_u symmetry show a non-negligible delocalization along with a reasonable energy overlap with the VB edge [these last levels have a higher contribution arising from surface carbons, see Fig. 3(a)] as can be inspected from the computed DOS in Fig. 2.

The quantum confinement effect on the spectral shift of the ZPL (ΔE_{ZPL}) as a function of the band-to-band-excitonic transition (ΔE_{EXC}) has the approximate relationship, according to the effective-mass approximation for a spherical nanocrystal [17,39,42],

$$\Delta E_{\text{ZPL}} \approx \frac{m_e^{*-1}}{m_e^{*-1} + m_h^{*-1}} \Delta E_{\text{EXC}}, \quad (1)$$

where m_e^* and m_h^* are the effective masses (in units of electron mass) of the electron and hole in the SiV-containing nanodiamond. The ${}^2E_g(e_u^4e_g^3) \rightarrow {}^2E_u(e_u^3e_g^4)$ excitations (as a weighted average of the first two excitations in Table I) as a function of the band-to-band-excitonic transition for the different dot sizes is plotted in Fig. 5. The $\Delta E_{\text{ZPL}}/\Delta E_{\text{EXC}}$ value is 0.04 , less than that in NV-doped nanodiamonds [22] and is significantly smaller than those for the free CB electron in diamond quantum dots. The observed size dependence of

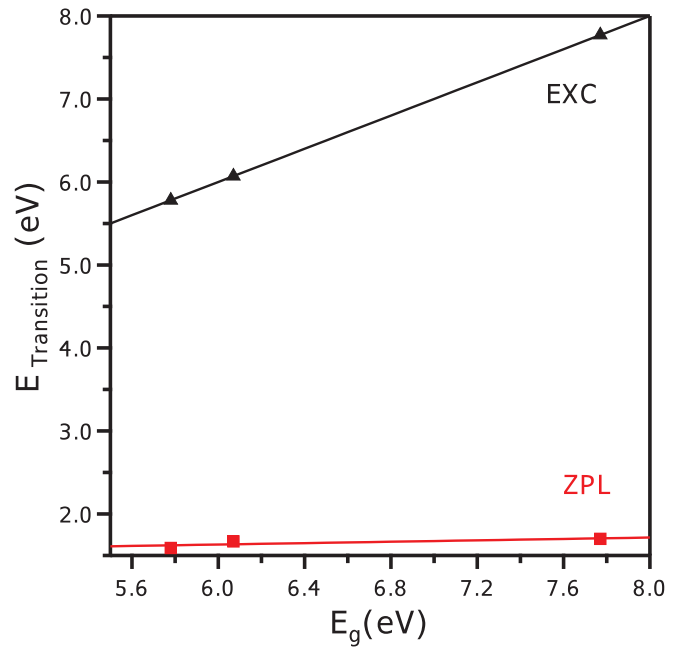


FIG. 5. TD-CAM-B3LYP/6-31 + +G(d, p) $\text{SiV } {}^2E_u(e_u^4e_g^3) \rightarrow {}^2E_u(e_u^3e_g^4)$ ZPL excitations as a function of the band-to-band-excitonic transition for the anionic SiV^- systems. Extrapolation of the ZPL energies gives a value of 1.38 eV for the bulk and the ratio between ΔE_{ZPL} and ΔE_{EXC} as the slope of the linear fit is 0.04 [the reported EXC energy (band gap) is reported as a HOMO/LUMO difference, which can underestimate the experimentally observed optical band gap as it has not been computed at the TDDFT level of theory and can be affected by the presence of surface defects in the experiment].

the ZPL is comparable with the one predicted using similar dimensions and level of theory [33]. Moreover, the quantitative analysis presented here suggests that the photoexcited electrons in the SiV ZPL excited states of diamonds are “heavier” than those in the pure diamond excitonic states.

C. Symmetry (or the lack of)

The two MOs of e_u symmetry have different spatial extents [i.e., different symmetries along the x and y directions, see Fig. 3(a)] and subsequently different overlaps with the empty MOs of e_g symmetry, showing different relative intensities in their transitions as can be inferred by inspecting computed oscillator strength values reported for the different sized SiV-doped nanodiamonds in Table I. By analyzing these values for the SiV *frozen* systems (right columns in Table I), an average splitting of ~ 0.27 eV is already noted for the computed ${}^2E_u(e_u^4e_g^3) \rightarrow {}^2E_u(e_u^3e_g^4)$ excitations. As mentioned before, although the SiV *frozen* conformation has an overall C_{3v} symmetry, both the asymmetry in the surface and the different spatial overlap of the filled MOs of e_u symmetry with the VB can be responsible for the energy splitting in the two ${}^2E_u(e_u^4e_g^3) \rightarrow {}^2E_u(e_u^3e_g^4)$ transitions even in these *frozen* conformations [see the different overlaps with the VB in Fig. 3(b)]. The asymmetric overlap between e_u MOs with the VB is, therefore, the key reason for both the excitonic behavior (analyzed in the previous paragraph) and the asymmetry of

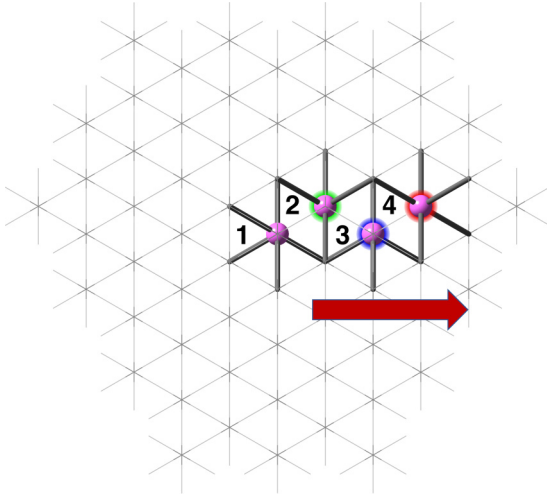


FIG. 6. Schematic layout of the four SiV positions in the $C_{180}SiH_{142}^-$ system used to investigate anisotropic effects on SiV midgap optical transitions.

the absorption peak in the visible range for the SiV-doped systems. A similar interpretation has been previously provided for silicon-doped nanodiamonds of similar dimensions [33].

The effect of lattice reorganization on the ${}^2E_u(e_u^4e_g^3) \rightarrow {}^2E_u(e_u^3e_g^4)$ excitations as a function of the system size can be also analyzed in Table I (from right to left). The geometry reorganization is responsible for an additional blueshift in vertical excitation energies from ~ 0.07 (first excitation) to ~ 0.25 eV (second excitation) with respect to the unrelaxed conformations. The degree of splitting of the two ${}^2E_u(e_u^4e_g^3) \rightarrow {}^2E_u(e_u^3e_g^4)$ excitations for the SiV *relaxed* systems are comparable to the ones computed for the SiV *frozen*, suggesting that the interactions of these levels with the VB band and surface are already significant to induce asymmetry in these excitations even in the SiV *frozen*-doped systems.

Since the relative position of the SiV defect with respect to the nanodiamond surface can further perturb the overall symmetry of the system, we inspected how the location of the SiV center within the nanodiamond can affect the SiV ZPL transitions. As the SiV center moves away from the C_{3v} (pseudolocal D_{3d} in SiV *frozen* systems) symmetry center, its global symmetry is no longer C_{3v} . As a result, the set of MOs of e_u and e_g symmetries as shown in Fig. 3(b) are even more energetically different due to the different interactions of the x and y subsets of the e_u and e_g MOs [see their asymmetric distributions in Fig. 3(b)] as the SiV moves closer to the surface (e.g., positions 2–4 in Fig. 6). The consequence of the symmetry breaking due to the defect position on ${}^2E_u(e_u^4e_g^3) \rightarrow {}^2E_u(e_u^3e_g^4)$ excitations is summarized in Table II. A splitting of ~ 400 meV of SiV midgap transitions is observed when the SiV moves away from the C_{3v} center of the nanodiamond for the SiV *frozen*. The magnitude of the splitting is not very sensitive to the defect position with respect to the surface, although the overall values show an overall 0.1-eV blueshift for the SiV positions closest to the surface (larger if the systems are allowed to relax as can be determined by looking at the values on the left in the table). This splitting of midgap transitions has been previously shown to be sensitive to the

TABLE II. TD-CAM-B3LYP/6-31 + $+G(d, p)$ midgap vertical excitation energies (e_u to e_g , β manifold) for the anionic SiV $^-$ systems (in eV) as a function of the SiV center position moving from the center (position 1) towards the surface (position 4) for the $C_{180}SiH_{142}^-$ system. Results are compared between the SiV *relaxed* (SiV center position is optimized, see the text) with the ones obtained by just inserting the SiV center by replacing the corresponding atoms (SiV *frozen*) in the center of the pure nanodiamond.

| | SiV <i>relaxed</i> | SiV <i>frozen</i> |
|------------|--------------------|-------------------|
| Position 1 | 1.59 | 1.51 |
| | 1.99 | 1.90 |
| Position 2 | 1.66 | 1.67 |
| | 2.07 | 2.07 |
| Position 3 | 1.69 | 1.67 |
| | 2.12 | 2.07 |
| Position 4 | 1.67 | 1.60 |
| | 2.05 | 2.00 |

defect position relative to the surface, but its absolute value for SiV defects appears to be larger than for the NV center [22]. Both the SiV $^-$ peak position and the broadening of the emission linewidth have experimentally been proved to be

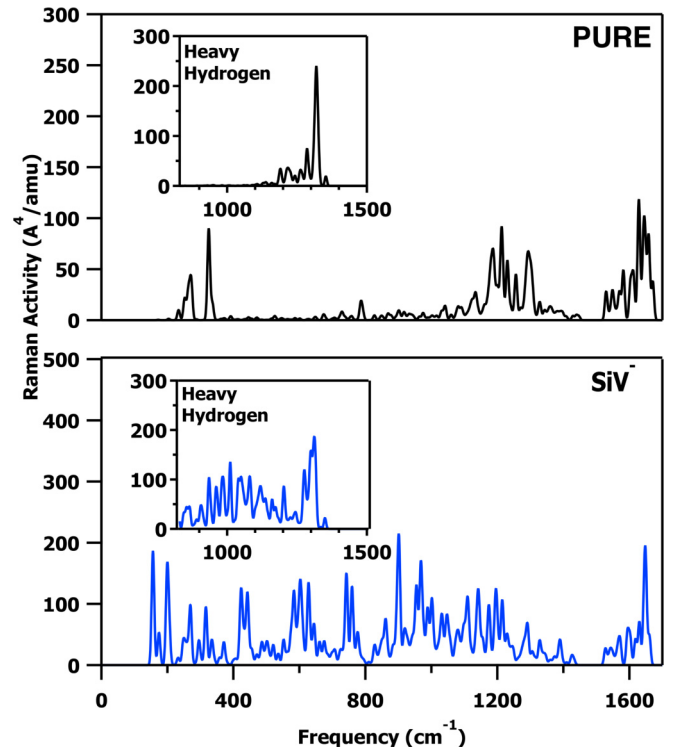


FIG. 7. CAM-B3LYP/6-31G(d) calculated Raman spectra for the ~ 1.2 -nm diameter pure $C_{121}H_{104}$ (black) and the reduced (isotopically averaged) SiV $^-$ $C_{119}SiH_{104}$ fully optimized nanodiamonds (blue). A Gaussian broadening has been applied with a full width half maximum value of 4 cm^{-1} . The insets of the spectral window originally overlapping with the H-C-H modes (from 800 to 1600 cm^{-1}) obtained using artificially heavy hydrogen atoms (100 amu) are reported for both spectra. The Raman spectrum for Si substitutional defect can be found in the Supplemental Information (Fig. S2) [79].

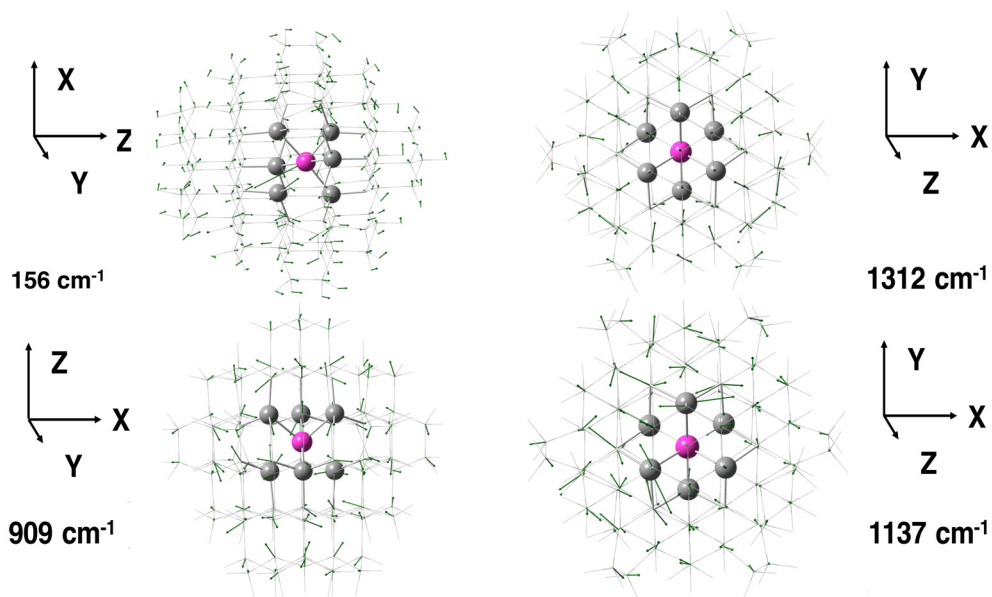


FIG. 8. Displacement vectors of the most representative normal modes for the ~ 1.2 -nm diameter $\text{SiV}^- \text{C}_{119}\text{SiH}_{104}$ -doped fully optimized nanodiamond. The modes within the 909 – 1137 - cm^{-1} energy range are represented using the heavy hydrogen approximation for clarity, whereas the lowest pictured mode at 156 cm^{-1} is shown with the regularly massed system. Representations of the individual modes are also provided in the Supplemental Material (Figs. S3 to S6) [79].

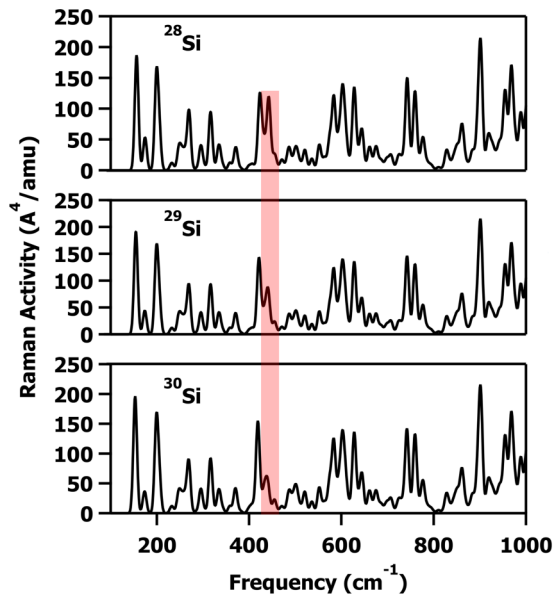
sensitive to either uniaxial stress or the position of the center within the matrix in a similar way to the predicted values (~ 200 meV in some observed broadenings) [83–85]. As the ZPL is sensitive to the surface reorganization and the size of the system, SiV centers can be effective probes of the global and local distortions, i.e., mechanical stress or pressure.

D. Vibrational analysis

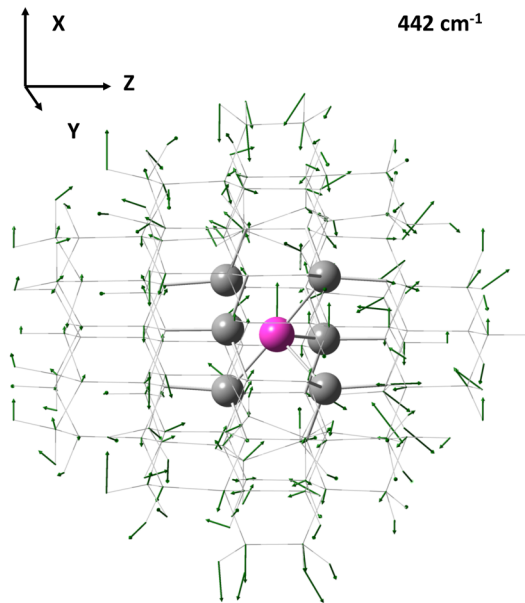
Vibrational spectroscopy can be very sensitive to the presence of defects since localized defects can strongly change the selection rules for infrared and Raman active modes. Presented in Fig. 7 are the Raman spectra for the 1.2 -nm pure (black) and reduced SiV^- (blue) nanodiamonds. Given the system size and the high computational cost of Raman calculations, a less expensive $6\text{-}31G(d)$ basis set was utilized for frequency and Raman intensity calculations. This choice is based on the observation that fully optimized geometries using $6\text{-}31 + G(d, p)$ and $6\text{-}31G(d)$ bases show negligible differences especially at the defect center. For the calculation of the vibrational response, it has been noted that, for large systems, this level of theory is sufficient [86–89], although Raman intensity can be improved with additional diffuse functions. The energy range discussed covers the region mostly affected by the presence of the SiV defects (the C-H stretching modes localized on the surface at $\gtrsim 3000$ cm^{-1} are not represented). Two distinctive regions can be located by observing the Raman spectrum: the region between 1200 and 1650 cm^{-1} , involving surface H-C-H bending motions covering the typical diamond Raman band around 1300 cm^{-1} (due to the lattice C-C stretching), and the low-frequency modes between ~ 150 and ~ 450 cm^{-1} , involving collective lattice breathing modes. The separation of these two regions has been shown to be

sensitive to both the size and the shape of nanodiamonds [90]. By introducing the SiV defect, an overall increase in the signal response in the region below 1100 cm^{-1} is observed. The main vibrational signatures of the presence of the SiV defect seem to be located around ~ 910 and ~ 156 cm^{-1} . These modes have a high contribution from the Si atom: The first are still collective stretching modes of the lattice in which C-Si are also strongly involved, whereas the lower-energy ones are the vacancy stretching breathing modes (see Fig. 8 for their representations). This last spectral region seems to be the most sensitive to the isotopic substitution of the silicon atom as can be inferred by the examination of Fig. 9(a) where the isotopic pure Raman spectra for the most abundant isotopes of silicon are reported (^{28}Si , ^{29}Si , and ^{30}Si from top to bottom of the left panel). A progressive redshift of ~ 1.5 cm^{-1} is observed for the peak around ~ 156 cm^{-1} for each increase in the silicon atomic mass. In addition, the breathing mode at ~ 442 cm^{-1} [marked in red in Fig. 9(a) and represented in Fig. 9(b)] strongly shows a decrease in intensity as an effect of the isotopic mass increment. Vibrational Raman responses associated with the anionic SiV^- and the Si substitutional defect were also compared. The substitutional defect was obtained by replacing a carbon atom close to the center of the ~ 1.2 -nm pure nanodiamond with a Si atom and optimizing the resulting structure. The SiV^- shows very distinct vibrational responses with respect to both the pure and the substitutional one (see Fig. S2 of the Supplemental Material [79]).

Unfortunately, the spectral region presenting the typical diamond Raman peak, involving the C-C lattice stretching motions reported at ~ 1330 cm^{-1} for bulk diamonds [91–93], is completely washed out by H-C-H bending motions due to the hydrogen passivation of the surface. This problem is solved by setting the atomic mass of hydrogen to



(a)



(b)

FIG. 9. (a) B3LYP/6-31G(d) isotopically pure calculated Raman spectra for the three most abundant [98] silicon isotopes ^{28}Si (92%), ^{29}Si (5%), and ^{30}Si (3%) from top to bottom of the left panel for the ~ 1.2 -nm-diameter $\text{SiV}^- \text{C}_{119}\text{SiH}_{104}^-$ fully optimized nanodiamond. (b) Displacement vectors of the most representative normal mode sensitive to the isotopic substitution.

a large value (100 amu), which corresponds effectively to shift away the overlapping features from the studied spectral window [48,90,94]. The obtained Raman spectra using heavy hydrogen atoms (from 800 to 1600 cm^{-1}) are reported in insets of Fig. 7. The pure nanodiamond presents a sharp peak around $\sim 1310 \text{ cm}^{-1}$ due to the C-C lattice stretching motions (see Fig. 8). This is the typical diamond Raman fingerprint and it is 20 cm^{-1} redshifted with respect the experimental bulk phonon band [90,94]. The SiV-doped spectrum shows a broadening of this peak where several lattice stretch-

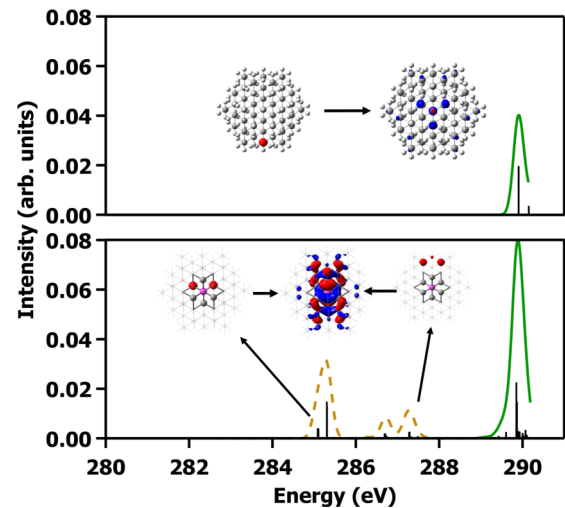


FIG. 10. TD-CAM-B3LYP/6-31++G(d,p) calculated XAS for the ~ 1.2 -nm-diameter pure $\text{C}_{121}\text{H}_{104}$ (top, 10 states), and the reduced $\text{SiV}^- \text{C}_{119}\text{SiH}_{104}^-$ (bottom, 103 states) nanodiamonds. Carbon core $1s \rightarrow e_g$ and $1s \rightarrow \sigma^*$ transitions are grouped in orange (dashed) and green (solid), respectively. A Gaussian broadening has been applied to the individual transitions labeled with black lines to form the spectra with a full width half maximum value of 0.12 eV, and a uniform shift of 12 eV has been applied to the spectra to align theoretical results with experimental values. Contour plots of the molecular orbitals responsible for the carbon K -edge transitions with the pseudo- C_{3v} axis parallel to the z axis (entering the figure) using an isodensity value of 0.025 are also represented.

ing C-C motions involving carbon atoms around the SiV are now gaining intensity due to the presence of the Si, related to changes in the polarizability for these modes. These results are in agreement with the broadening observed for Raman spectra of Si-doped diamonds [95–97].

E. X-ray absorption spectroscopy

X-ray absorption spectroscopy (XAS) is extensively used for sample analysis since it is a highly element specific spectroscopic technique. The K -edge feature in the XAS is due to the excitations involving $1s$ core electrons and the virtual valence molecular orbitals; for these reasons the structure of these peaks can provide useful information on the local order around the absorbing centers [99–102]. The resulting carbon K -edge x-ray absorption spectra for the ~ 1.2 -nm-diameter pure $\text{C}_{121}\text{H}_{104}$ and the reduced $\text{SiV}^- \text{C}_{119}\text{SiH}_{104}^-$ nanodiamonds are reported in Fig. 10. The pure nanodiamond presents a clear absorption peak starting at 290 eV due to the well-studied $1s \rightarrow \sigma^*$ transitions. As the SiV is introduced, several pre-edge transitions start to appear around 284–285 eV. The main peak at $\sim 290 \text{ eV}$ for the Si-doped systems is still due to several $1s \rightarrow \sigma^*$ electronic transitions as can be inferred by inspecting the MOs responsible for them in both the pure and the doped systems (see their representations in Fig. 10). The pre-edge peaks around 285 eV are due to the presence of the SiV defects, arising from several carbon $1s \rightarrow e_g$ transitions (see Fig. 10). These analyses suggest that the pre-edge feature experimentally observed at $\sim 285 \text{ eV}$ can be a signature of the presence of defects (i.e., SiV centers).

Although these carbon transitions are typically ascribed to sp^2 carbon atoms lying on the surface [48], it should be noted that these are also available to the dangling bonds surrounding carbon vacancies. However, in defects, such as NV and SiV, the presence of heteroatoms influences the $1s \rightarrow e_g$ carbon transition. Thus, the location of the carbon K -edge pre-edge features can be used to probe the presence of different dopants in diamonds [38].

IV. CONCLUSION

In this paper, the midgap states introduced by localized defects have been shown to affect UV-vis, x-ray, and vibrational transitions in diamonds approaching the nanoscale. Using group theory and the DFT electronic structure, we showed how the midgap states introduced by the reduced SiV center have a non-negligible overlap with the diamond VB and CB. This explains the size-dependent nature of the computed SiV ZPL, and we predict an effective excitonic mass for these transitions comparable to charge-transfer excitations in NV-doped nanodiamonds. We also found the ZPL to be sensitive both to the lack of symmetry in all systems analyzed and to the defect position by measuring the band position during the defect migration towards the surface. Two diamond Raman vibrational spectrum regions are predicted to be significantly modified by the SiV center: The large amplitude breathing ($120\text{--}450\text{-cm}^{-1}$) and the stretching ($800\text{--}1400\text{-cm}^{-1}$)

motions of the lattice. Core $1s \rightarrow e_g$ (midgap states) transitions introduced by SiV centers are predicted to be responsible for the occurrence of pre-edge peaks in the computed carbon K -edge x-ray absorption spectrum for nanodiamonds, showing how this spectral region (~ 285 eV) can be influenced by the presence of localized defects. This paper provides an important *ab initio* analysis of the electronic and vibrational structures of semiconductors in the presence of midgap states due to localized defects, providing a molecular description of the spectroscopic changes in doped systems.

ACKNOWLEDGMENTS

The development of the energy-specific TDDFT method for computing XAS spectra is supported by the NSF (Grant No. CHE-1565520 to X.L.). The study of defects in nanodiamonds is supported by the University of Washington Molecular Engineering Materials Center (Grant No. DMR-1719797), NSF (Grant No. CHE-1464497 to X.L., and Grant No. NSF-CAREER 1555007 to P.P.). This work was facilitated through the use of the advanced computational, storage, and networking infrastructure provided by the Hyak supercomputer system and funded by the STF at the University of Washington and the National Science Foundation (Grant No. MRI-1624430).

A.P. and R.A.B. contributed equally to this work.

-
- [1] D. Mocatta, G. Cohen, J. Schattner, O. Millo, E. Rabani, and U. Banin, *Science* **332**, 77 (2011).
 - [2] M. Sytnyk, R. Kirchschrager, M. I. Bodnarchuk, D. Primetzhofner, D. Krieger, H. Enser, J. Stangl, P. Bauer, M. Voith, A. W. Hassel, F. Krumeich, F. Ludwig, A. Meingast, G. Kothleitner, M. V. Kovalenko, and W. Heiss, *Nano Lett.* **13**, 586 (2013).
 - [3] S. Pezzagna, D. Rogalla, D. Wildanger, J. Meijer, and A. Zaitsev, *New J. Phys.* **13**, 035024 (2011).
 - [4] J. Eilers, E. Groeneveld, C. de Mello Donegá, and A. Meijerink, *J. Phys. Chem. Lett.* **3**, 1663 (2012).
 - [5] F. Dolde, M. W. Doherty, J. Michl, I. Jakobi, B. Naydenov, S. Pezzagna, J. Meijer, P. Neumann, F. Jelezko, N. B. Manson, and J. Wrachtrup, *Phys. Rev. Lett.* **112**, 097603 (2014).
 - [6] J. L. Stein, M. I. Steimle, M. W. Terban, A. Petrone, S. J. L. Billinge, X. Li, and B. M. Cossairt, *Chem. Mater.* **29**, 7984 (2017).
 - [7] M. E. Levinshtein, S. L. Rumyantsev, and M. Shur, *Handbook Series on Semiconductor Parameters: Si, Ge, C (Diamond), GaAs, GaP, GaSb, InAs, InP, InSb* (World Scientific, Singapore, 1996).
 - [8] K. Holt, *Philos. Trans. R. Soc., A* **365**, 2845 (2007).
 - [9] G. Balasubramanian, I. Y. Chan, R. Kolesov, M. Al-Hmoud, J. Tisler, C. Shin, C. Kim, A. Wojcik, P. Hemmer, A. Krueger, T. Hanke, A. Leitenstorfer, R. Bratschitsch, F. Jelezko, and J. Wrachtrup, *Nature (London)* **455**, 648 (2008).
 - [10] Y.-R. Chang, H.-Y. Lee, K. Chen, C.-C. Chang, D.-S. Tsai, C.-C. Fu, T.-S. Lim, Y.-K. Tzeng, C.-Y. Fang, C.-C. Han, H.-C. Chang, and W. Fann, *Nat. Nanotechnol.* **3**, 284 (2008).
 - [11] L. P. McGuinness, Y. Yan, A. Stacey, D. A. Simpson, L. T. Hall, D. Maclaurin, S. Prawer, P. Mulvaney, J. Wrachtrup, F. Caruso, R. E. Scholten, and L. C. L. Hollenberg, *Nat. Nanotechnol.* **6**, 358 (2011).
 - [12] P. J. Pauzauskie, J. C. Crowhurst, M. A. Worsley, T. A. Laurence, A. L. D. Kilcoyne, Y. Wang, T. M. Willey, K. S. Visbeck, S. C. Fakra, W. J. Evans, J. M. Zaug, and J. H. Satcher, *Proc. Natl. Acad. Sci. USA* **108**, 8550 (2011).
 - [13] S. Manandhar, P. B. Roder, J. L. Hanson, M. Lim, B. E. Smith, A. Mann, and P. J. Pauzauskie, *J. Mater. Res.* **29**, 2905 (2014).
 - [14] N. Aslam, M. Pfender, P. Neumann, R. Reuter, A. Zappe, F. F. de Oliveira, A. Denisenko, H. Sumiya, S. Onoda, J. Isoya, and J. Wrachtrup, *Science* **357**, 67 (2017).
 - [15] C. Kittel and P. McEuen, *Introduction to Solid State Physics* (Wiley, NY, 1976), Vol. 8.
 - [16] N. Ashcroft and N. Mermin, *Solid State Physics* (Saunders College, Philadelphia, PA, 1976).
 - [17] L. E. Brus, *J. Chem. Phys.* **80**, 4403 (1984).
 - [18] M. G. Bawendi, M. L. Steigerwald, and L. E. Brus, *Annu. Rev. Phys. Chem.* **41**, 477 (1990).
 - [19] T. Karin, S. Dunham, and K.-M. Fu, *Appl. Phys. Lett.* **105**, 053106 (2014).
 - [20] M. Drake, E. Scott, and J. Reimer, *New J. Phys.* **18**, 013011 (2015).
 - [21] K. Sasaki, E. E. Kleinsasser, Z. Zhu, W.-D. Li, H. Watanabe, K.-M. C. Fu, K. M. Itoh, and E. Abe, *Appl. Phys. Lett.* **110**, 192407 (2017).
 - [22] A. Petrone, J. J. Goings, and X. Li, *Phys. Rev. B* **94**, 165402 (2016).

- [23] M. Leifgen, T. Schröder, F. Gödeke, R. Riemann, V. Metillon, E. Neu, C. Hepp, C. Arend, C. Becher, K. Lauritsen, and O. Benson, *New J. Phys.* **16**, 023021 (2014).
- [24] E. Neu, D. Steinmetz, J. Riedrich-Möller, S. Gsell, M. Fischer, M. Schreck, and C. Becher, *New J. Phys.* **13**, 025012 (2011).
- [25] A. Dietrich, K. D. Jahnke, J. M. Binder, T. Teraji, J. Isoya, L. J. Rogers, and F. Jelezko, *New J. Phys.* **16**, 113019 (2014).
- [26] M. J. Crane, A. Petrone, R. A. Beck, M. B. Lim, X. Zhou, X. Li, R. M. Stroud, and P. J. Pauzuskie, [arXiv:1804.00350](https://arxiv.org/abs/1804.00350).
- [27] J. P. Goss, R. Jones, S. J. Breuer, P. R. Briddon, and S. Öberg, *Phys. Rev. Lett.* **77**, 3041 (1996).
- [28] J. P. Goss, P. R. Briddon, and M. J. Shaw, *Phys. Rev. B* **76**, 075204 (2007).
- [29] A. S. Zyubin, A. Mebel, M. Hayashi, H. C. Chang, and S. H. Lin, *J. Comput. Chem.* **30**, 119 (2009).
- [30] A. Gali and J. R. Maze, *Phys. Rev. B* **88**, 235205 (2013).
- [31] L. J. Rogers, K. D. Jahnke, M. W. Doherty, A. Dietrich, L. P. Mc Guinness, C. Müller, T. Teraji, H. Sumiya, J. Isoya, N. B. Manson, and F. Jelezko, *Phys. Rev. B* **89**, 235101 (2014).
- [32] T. Müller, C. Hepp, B. Pingault, E. Neu, S. Gsell, M. Schreck, H. Sternschulte, D. Steinmüller-Nethl, C. Becher, and M. Atatüre, *Nat. Commun.* **5**, 3328 (2014).
- [33] I. I. Vlasov, A. A. Shiryaev, T. Rendler, S. Steinert, S.-Y. Lee, D. Antonov, M. Vörös, F. Jelezko, A. V. Fisenko, L. F. Semjonova, J. Biskupek, U. Kaiser, O. I. Lebedev, I. Sildos, P. R. Hemmer, V. I. Konov, A. Gali, and J. Wrachtrup, *Nat. Nanotechnol.* **9**, 54 (2014).
- [34] C. D. Clark, H. Kanda, I. Kiflawi, and G. Sittas, *Phys. Rev. B* **51**, 16681 (1995).
- [35] E. Neu, C. Hepp, M. Hauschild, S. Gsell, M. Fischer, H. Sternschulte, D. Steinmüller-Nethl, M. Schreck, and C. Becher, *New J. Phys.* **15**, 043005 (2013).
- [36] C. Hepp, T. Müller, V. Waselowski, J. N. Becker, B. Pingault, H. Sternschulte, D. Steinmüller-Nethl, A. Gali, J. R. Maze, M. Atatüre, and C. Becher, *Phys. Rev. Lett.* **112**, 036405 (2014).
- [37] G. Thiering and A. Gali, *Phys. Rev. X* **8**, 021063 (2018).
- [38] S. L. Chang, A. S. Barnard, C. Dwyer, C. B. Boothroyd, R. K. Hocking, E. Ōsawa, and R. J. Nicholls, *Nanoscale* **8**, 10548 (2016).
- [39] E. Badaeva, C. M. Isborn, Y. Feng, S. T. Ochsenbein, D. R. Gamelin, and X. Li, *J. Phys. Chem. C* **113**, 8710 (2009).
- [40] R. Beaulac, Y. Feng, J. W. May, E. Badaeva, D. R. Gamelin, and X. Li, *Phys. Rev. B* **84**, 195324 (2011).
- [41] J. W. May, R. J. McMorris, and X. Li, *J. Phys. Chem. Lett.* **3**, 1374 (2012).
- [42] J. W. May, J. Ma, E. Badaeva, and X. Li, *J. Phys. Chem. C* **118**, 13152 (2014).
- [43] J. J. Goings, A. M. Schimpf, J. W. May, R. W. Johns, D. R. Gamelin, and X. Li, *J. Phys. Chem. C* **118**, 26584 (2014).
- [44] B. Peng, J. W. May, D. R. Gamelin, and X. Li, *J. Phys. Chem. C* **118**, 7630 (2014).
- [45] L. R. Bradshaw, J. W. May, J. L. Dempsey, X. Li, and D. R. Gamelin, *Phys. Rev. B* **89**, 115312 (2014).
- [46] E. Q. Chong, D. B. Lingerfelt, A. Petrone, and X. Li, *J. Phys. Chem. C* **120**, 19434 (2016).
- [47] D. C. Gary, A. Petrone, X. Li, and B. M. Cossairt, *Chem. Commun.* **53**, 161 (2017).
- [48] R. Beck, A. Petrone, J. M. Kasper, M. J. Crane, P. J. Pauzuskie, and X. Li, *J. Phys. Chem. C* **122**, 8573 (2018).
- [49] M. W. Wong, *Chem. Phys. Lett.* **256**, 391 (1996).
- [50] V. Barone, J. Bloino, and M. Biczysko, *Phys. Chem. Chem. Phys.* **12**, 1092 (2010).
- [51] A. Petrone, D. B. Lingerfelt, D. B. Williams-Young, and X. Li, *J. Phys. Chem. Lett.* **7**, 4501 (2016).
- [52] G. Donati, D. B. Lingerfelt, A. Petrone, N. Rega, and X. Li, *J. Phys. Chem. A* **120**, 7255 (2016).
- [53] D. B. Lingerfelt, D. B. Williams-Young, A. Petrone, and X. Li, *J. Chem. Theory Comput.* **12**, 935 (2016).
- [54] N. R. Greiner, D. S. Phillips, J. D. Johnson, and F. Volk, *Nature (London)* **333**, 440 (1988).
- [55] V. Y. Dolmatov, *Russ. Chem. Rev.* **76**, 339 (2007).
- [56] E. Ōsawa, *Pure Appl. Chem.* **80**, 1365 (2008).
- [57] K. Takahashi, A. Yoshikawa, and A. Sandhu, *Wide Bandgap Semiconductors: Fundamental Properties and Modern Photonic and Electronic Devices* (Springer, New York, 2007).
- [58] S. S. Moliver, *Tech. Phys.* **48**, 1449 (2003).
- [59] T. Feng and B. D. Schwartz, *J. Appl. Phys.* **73**, 1415 (1993).
- [60] G. Thiering and A. Gali, *Phys. Rev. B* **92**, 165203 (2015).
- [61] M. J. Frisch, G. W. Trucks, H. B. Schlegel, G. E. Scuseria, M. A. Robb, J. R. Cheeseman, G. Scalmani, V. Barone, G. A. Petersson, H. Nakatsuji, X. Li, M. Caricato, A. V. Marenich, J. Bloino, B. G. Janesko, R. Gomperts, B. Mennucci, H. P. Hratchian, J. V. Ortiz, A. F. Izmaylov, J. L. Sonnenberg, D. Williams-Young, F. Ding, F. Lipparini, F. Egidi, J. Goings, B. Peng, A. Petrone, T. Henderson, D. Ranasinghe, V. G. Zakrzewski, J. Gao, N. Rega, G. Zheng, W. Liang, M. Hada, M. Ehara, K. Toyota, R. Fukuda, J. Hasegawa, M. Ishida, T. Nakajima, Y. Honda, O. Kitao, H. Nakai, T. Vreven, K. Throssell, J. A. Montgomery, Jr., J. E. Peralta, F. Ogliaro, M. J. Bearpark, J. J. Heyd, E. N. Brothers, K. N. Kudin, V. N. Staroverov, T. A. Keith, R. Kobayashi, J. Normand, K. Raghavachari, A. P. Rendell, J. C. Burant, S. S. Iyengar, J. Tomasi, M. Cossi, J. M. Millam, M. Klene, C. Adamo, R. Cammi, J. W. Ochterski, R. L. Martin, K. Morokuma, O. Farkas, J. B. Foresman, and D. J. Fox, *Gaussian Development Version Revision I.10++* (Gaussian Inc., Wallingford, CT, 2016).
- [62] A. D. Becke, *J. Chem. Phys.* **98**, 5648 (1993).
- [63] C. Lee, W. Yang, and R. G. Parr, *Phys. Rev. B* **37**, 785 (1988).
- [64] B. Miehlisch, A. Savin, H. Stoll, and H. Preuss, *Chem. Phys. Lett.* **157**, 200 (1989).
- [65] T. Yanai, D. P. Tew, and N. C. Handy, *Chem. Phys. Lett.* **393**, 51 (2004).
- [66] M. Vörös and A. Gali, *Phys. Rev. B* **80**, 161411(R) (2009).
- [67] T. Demján, M. Vörös, M. Palummo, and A. Gali, *J. Chem. Phys.* **141**, 064308 (2014).
- [68] M. Kaviani, P. Deák, B. Aradi, T. Frauenheim, J.-P. Chou, and A. Gali, *Nano Lett.* **14**, 4772 (2014).
- [69] C.-K. Lin, Y.-H. Wang, H.-C. Chang, M. Hayashi, and S. H. Lin, *J. Chem. Phys.* **129**, 124714 (2008).
- [70] A. Gali, *Phys. Status Solidi B* **248**, 1337 (2011).
- [71] N. Mardirossian, J. A. Parkhill, and M. Head-Gordon, *Phys. Chem. Chem. Phys.* **13**, 19325 (2011).
- [72] A. D. Laurent and D. Jacquemin, *Int. J. Quant. Chem.* **113**, 2019 (2017).
- [73] R. Derian, K. Tokár, B. Somogyi, A. Gali, and I. Štich, *J. Chem. Theory Comput.* **13**, 6061 (2017).

- [74] M. E. Casida, in *Recent Advances in Density Functional Methods:(Part I)*, edited by D. P. Chong (World Scientific, Singapore, 1995), Vol. 1, pp. 155–193.
- [75] A. Dreuw and M. Head-Gordon, *Chem. Rev.* **105**, 4009 (2005).
- [76] R. E. Stratmann, G. E. Scuseria, and M. J. Frisch, *J. Chem. Phys.* **109**, 8218 (1998).
- [77] W. Liang, S. A. Fischer, M. J. Frisch, and X. Li, *J. Chem. Theory Comput.* **7**, 3540 (2011).
- [78] P. J. Lestrangé, P. D. Nguyen, and X. Li, *J. Chem. Theory Comput.* **11**, 2994 (2015).
- [79] See Supplemental Material at <http://link.aps.org/supplemental/10.1103/PhysRevB.98.205405> for the change in the SiV structure for full-diamond optimization, the isotropic effects of silicon on the Raman spectroscopy, and enlarged images of the normal modes displayed in Fig. 8.
- [80] H.-P. Komsa, T. T. Rantala, and A. Pasquarello, *Phys. Rev. B* **86**, 045112 (2012).
- [81] S. Vepřek, *Thin Solid Films* **297**, 145 (1997).
- [82] E. Badaeva, Y. Feng, D. R. Gamelin, and X. Li, *New J. Phys.* **10**, 055013 (2008).
- [83] H. Sternschulte, K. Thonke, J. Gerster, W. Limmer, R. Sauer, J. Spitzer, and P. Münzinger, *Diamond Relat. Mater.* **4**, 1189 (1995).
- [84] E. Neu, M. Fischer, S. Gsell, M. Schreck, and C. Becher, *Phys. Rev. B* **84**, 205211 (2011).
- [85] S. W. Brown and S. C. Rand, *J. Appl. Phys.* **78**, 4069 (1995).
- [86] S. Salustro, A. Erba, C. M. Zicovich-Wilson, Y. Noël, L. Maschio, and R. Dovesi, *Phys. Chem. Chem. Phys.* **18**, 21288 (2016).
- [87] J. Bielecki and E. W. Lipiec, *J. Bioinf. Comput. Biol.* **14**, 1650002 (2016).
- [88] J. R. Cheeseman and M. J. Frisch, *J. Chem. Theory Comput.* **7**, 3323 (2011).
- [89] F. Billes, *J. Mol. Struct.* **339**, 15 (1995).
- [90] J. Filik, J. N. Harvey, N. L. Allan, P. W. May, J. E. P. Dahl, S. Liu, and R. M. K. Carlson, *Phys. Rev. B* **74**, 035423 (2006).
- [91] S. Praver and R. J. Nemanich, *Proc. R. Soc. London, Ser. A* **362**, 2537 (2004).
- [92] J. Cebik, J. K. McDonough, F. Peerally, R. Medrano, I. Neitzel, Y. Gogotsi, and S. Osswald, *Nanotechnol.* **24**, 205703 (2013).
- [93] V. I. Korepanov, H. o Hamaguchi, E. Osawa, V. Ermolenkov, I. K. Lednev, B. J. Etzold, O. Levinson, B. Zouzman, C. P. Epperla, and H.-C. Chang, *Carbon* **121**, 322 (2017).
- [94] W. Li, S. Irle, and H. A. Witek, *ACS Nano* **4**, 4475 (2010).
- [95] G. Wan, P. Yang, R. K. Fu, Y. Mei, T. Qiu, S. Kwok, J. P. Ho, N. Huang, X. Wu, and P. K. Chu, *Diamond Relat. Mater.* **15**, 1276 (2006).
- [96] S.-l. Chen, S. Bin, J.-G. Zhang, W. Liang, and F.-H. Sun, *Trans. Nonferrous Met. Soc. China* **22**, 3021 (2012).
- [97] Y.-X. Cui, J.-G. Zhang, F.-H. Sun, and Z.-M. Zhang, *Trans. Nonferrous Met. Soc. China* **23**, 2962 (2013).
- [98] M. Berglund and M. E. Wieser, *Pure Appl. Chem.* **83**, 397 (2011).
- [99] H. Moseley, *Lond. Edinb. Dubl. Philos. Mag.* **26**, 1024 (1913).
- [100] H. Moseley, *Lond. Edinb. Dubl. Philos. Mag.* **27**, 703 (1914).
- [101] J. Stöhr, *NEXAFS Spectroscopy* (Springer-Verlag, Berlin/Heidelberg, 1992).
- [102] A. Nilsson and L. G. M. Pettersson, *Surf. Sci. Rep.* **55**, 49 (2004).